Assessing the Energetics of Spinning Binary Black Hole Systems

Serguei Ossokine and Tim Dietrich
Max Planck Institute for Gravitational Physics (Albert Einstein Institute), Am Mühlenberg 1, Potsdam-Golm, 14476, Germany

Evan Foley, Reza Katebi, and Geoffrey Lovelace
Gravitational Wave Physics and Astronomy Center, California State University, Fullerton, Fullerton, California 92834, USA

(Dated: June 10, 2018)

In this work we study the dynamics of spinning binary black hole systems in the strong field regime. For this purpose we extract from numerical relativity simulations the binding energy, specific orbital angular momentum, and gauge-invariant orbital frequency. The goal of our work is threefold: First, we extract the individual spin contributions to the binding energy, in particular the spin-orbit, spin-spin, and cubic-in-spin terms. Second, we compare our results with predictions from waveform models and find that while post-Newtonian approximants are not capable of representing the dynamics during the last few orbits before merger, there is good agreement between our data and effective-one-body approximants as well as the numerical relativity surrogate models. Finally, we present phenomenological representations for the binding energy for non-spinning systems with mass ratios up to $q = 10$ and for the spin-orbit interaction for mass ratios up to $q = 8$ obtaining accuracies of $\lesssim 0.1\%$ and $\lesssim 6\%$, respectively.

PACS numbers: 04.25.D-, 04.30.Db, 04.70.Bw, 97.60.Lf

I. INTRODUCTION

With the direct detection of gravitational waves (GWs) from a binary black hole (BBH) system in 2015, Advanced LIGO ushered in the era of gravitational wave astronomy [1]. Since then, several detections have been made [2–5], including the spectacular observation of both GWs and electromagnetic radiation from a binary neutron star merger [6]. Due to the increasing sensitivity of the advanced detectors, an increasing number of detections is expected in the third observing run [7]. To interpret the large number of detections and extract astrophysical properties of the systems it is more important than ever to construct accurate models of merging compact binary systems.

In recent years, a large effort has been made to improve the modeling of the GW signal, leading to rapid progress in the field. Currently, there are at least three routes for constructing state-of-art waveform models: by directly using numerical relativity (NR) simulations and interpolating between those to obtain generic waveforms [8, 9]; by calibrating to NR waveforms following a phenomenological approach, e.g. [10–12]; or by combining analytical information from post-Newtonian (PN) theory(see [13] and references therein), with NR results in form of the effective-one-body (EOB) description [14–34].

In this paper we do not focus on the gravitational waveform; instead, we examine the global dynamics in terms of gauge-invariant quantities. In particular we study the binding energy E, specific orbital angular momentum ℓ, and the gauge-invariant orbital frequency $\hat{\Omega}$, see [30, 35]. Those quantities can be constructed from the strain by computing the radiated energy and angular momentum. An example of this calculation is given in Fig. 1. From the GW strain (top panel), we compute the energy and angular momentum emitted by the system (middle panel). From these, we construct gauge-invariant quantities: E and $\hat{\Omega}$ as a function of ℓ (bottom panel). Considering the marked times, one finds that due to the emission of energy and angular momentum, E and ℓ decrease over time, while the orbital frequency $\hat{\Omega}$ increases. The top panel shows that the dimensionless frequency $M\hat{\Omega}$ is half the frequency of the GW. Consequently, during the ringdown, $\hat{\Omega}$ can be interpreted as the main emission frequency of the quasi-normal modes.

Although the evolution of $E, \ell, \hat{\Omega}$ incorporates nonadiabatic effects, those are practically negligible during the inspiral until the LSO [35]. Thus, investigation of $E, \ell, \hat{\Omega}$ permits a direct probe of the conservative dynamics of a BBH in a highly relativistic regime. Not only does this improve our understanding of the inspiral dynamics, but it also allows us to study the influence of the mass ratio separately from those of the spin-orbit, spin-spin, and cubic-in-spin terms.

In this article, we focus primarily on three tasks: (i) extracting (up to our knowledge) for the first time different contributions to the binding energy from NR simulations of BBHs; (ii) comparing our results to state-of-the-art waveform models to test their accuracy; and (iii) proposing phenomenological fits, including unknown higher order PN coefficients, to constrain the binding energy for aligned spin systems.

The structure of the paper is as follows. In Sec. II we describe the employed numerical methods, the construction of gauge-invariant quantities, and numerical errors. In Sec. III we present the results for non-spinning configurations accessing the effect of the mass-ratio on the dynamics. In Sec. IV we study spinning-equal mass con-

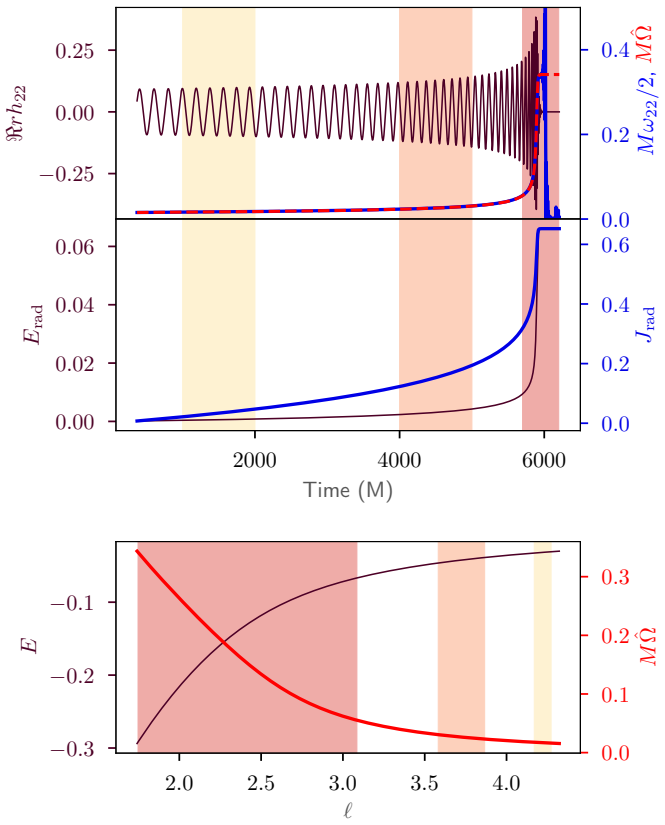

FIG. 1. Top: gravitational wave strain h (thin purple line) and gravitational wave frequency (thick blue line) as a function of time. The dashed red line is the gauge invariant frequency $M\hat{\Omega}$. Middle: emitted energy (thin purple lines) and angular momentum (thick blue line) Bottom: the binding energy E and the orbital frequency $M\hat{\Omega}$ as a function of the specific orbital angular momentum ℓ. All quantities are plotted for an equal mass BBH system with dimensionless spin $\chi_1 = \chi_2 = 0.6$.

figurations and extract the individual spin components up to cubic-in-spin terms. Sec. V presents results for generic non-precessing systems. We conclude in Sec. VI. In Appendix A we extract spin orbit and spin-spin contribution with an alternative approach to Sec. IV, using only two different simulations per spin magnitude. In Appendix B we list the studied NR simulations.

Throughout the paper we employ geometric units with $G = c = 1$.

II. METHODS

A. Simulation method

In this article, we restrict ourselves to non-precessing configurations leaving precession for a future work. The studied NR simulations are produced with the Spectral Einstein Code (`SpEC`) [36–39] and are publicly available in the SXS catalogue [40, 41].

`SpEC` is a multi-domain, pseudospectral collocation code for the simulation of compact object binary spacetimes. Conformally curved initial data [42] are constructed in the extended-conformal-thin-sandwich formalism [43] using a pseudo-spectral elliptic solver [44]. Dynamical evolutions use a first order formulation [45] of the generalized harmonic formulation of Einstein's equations [46, 47] in the damped harmonic gauge [48]. `SpEC` uses a dual frame method [37, 49] to solve Einstein's equations based on explicit coordinate transformations. These map a set of inertial (physical) coordinates, in which the BHs orbit and approach each other, to a set of grid coordinates, in which the BHs remain at fixed coordinate locations. To handle the BH singularity, dynamical excision is used [49, 50]. An adaptive mesh refinement, which adjusts both the order of the spectral basis functions as well as the number of subdomains, is employed to achieve the desired truncation error, see [51]. `SpEC` has been successfully employed to simulate a large variety of physical systems; see, among others [9, 39, 41, 52–54]).

B. Constructing binding energy curves

To extract the reduced binding energy and the specific angular momentum from our BBH simulations, we compute the energy and angular momentum flux as described in [55]. The binding energy itself is defined as

$$E_b = \frac{E_{\rm ADM}(t=0) - E_{\rm rad} - M}{\mu}, \tag{1}$$

with $\mu = m_1 m_2/M$, where $E_{\rm ADM}$ is extracted at the beginning of the simulation $t = 0$. The dimensionless angular momentum is

$$j = \frac{|\mathbf{J}_{\rm ADM}(t=0) - \mathbf{J}_{\rm rad}|}{M\mu} \tag{2}$$

from which we can construct the dimensionless orbital angular momentum

$$\ell = \frac{|\mathbf{J}_{\rm ADM} - \mathbf{S_1} - \mathbf{S_2} - \mathbf{J}_{\rm rad}|}{M\mu}. \tag{3}$$

For spin-aligned/anti-aligned cases, $\mathbf{J}_{\rm ADM}, \mathbf{S_1}, \mathbf{S_2}, \mathbf{J}_{\rm rad}$ reduce to $J^z_{\rm ADM}, S^z_1, S^z_2, J^z_{\rm rad}$ respectively, since the orbital plane is identical to the x-y-plane.

The presence of junk radiation in our simulations causes an ambiguous shift of the curves; thus, as outlined in Ref. [28, 30], the binding energy curves must be further processed. The first step involves a vectorial shift in the $E - j$ plane, such that the curve passes through the final values of mass and spin of the merger remnant. This can be done in a way that eliminates the need of ADM quantities entirely. Indeed, letting

$(\tilde{E}, \tilde{j}) \equiv (E + \Delta E, j + \Delta j)$, and requiring that at the final time t_f, the curve passes through the point given by the mass M_f and spin S_f of the final black hole, $(E(t_f) + \Delta E, j(t_f) + \Delta j) = (M_f, S_f)$, it follows readily that $\Delta E = M_f - E(t_f) = M_f - E_{ADM} + E_{rad}(t_f)$. Consequently, $\tilde{E}(t) = E_{\rm rad}(t_f) - E_{\rm rad}(t) + M_f$, and similarly for j. For convenience we work exclusively with ℓ instead of j, since all the cases considered in this paper are non-precessing and difference between the two quantities is equivalent to a shift by a constant under the assumption that the spins of the individual black holes stay constant.

As an example, Figure 2 shows $E - \ell$ curves for an equal mass binary, with spins $\chi_1 = 0.6$, $\chi_2 = 0.6$ from NR (blue dotted line), and the non-precessing EOB model [34] (green dashed line), which we hereafter denote as SEOBNR [1]. Although the overall agreement is good, it is obvious that an offset between the EOB and the NR curves exists even in the early inspiral, at a time where the EOB description is expected to give accurate results. We assume that there are at least two reasons for this offset: (i) parts of the unresolved junk radiation imprint on the $E - \ell$ curves and can not be eliminated with a single shift $(\Delta E, \Delta \ell)$; (ii) there are extrapolation errors in the ringdown of higher modes. To resolve these issues, we perform an additional shift of the NR curve, aligning it with the EOB curve early in the inspiral. This is done by minimizing the difference in the binding energy over the interval $[0.94, 0.98]\ell_{\rm max}$, where $\ell_{\rm max}$ is the maximum value of ℓ in the NR data, after junk radiation has been removed. The shifted NR curve (purple solid line in Fig. 2) now agrees better with the EOB curve. A similar approach to construct binding energy curves from SpEC data was used in [30].

From $E(\ell)$, we compute the gauge-invariant frequency

$$M\hat{\Omega} \equiv \frac{\partial E}{\partial \ell}. \tag{4}$$

which corresponds to the orbital frequency for circular orbits in the adiabatic regime. We apply a Savitzky-Golay filter to eliminate oscillations due to residual eccentricity and numerical noise. From $M\hat{\Omega}$ it is possible to define the post-Newtonian parameter

$$x \equiv (M\hat{\Omega})^{2/3}. \tag{5}$$

C. Extracting individual contributions to the binding energy

In order to gain insight into the role of different spin interactions during the BBH coalescence, we make the assumption that

$$E \approx E_0 + E_{SO} + E_{S^2} + E_{SS} + E_{S^3} + E_{S^2S} + \mathcal{O}(S^4)\ ; \tag{6}$$

[1] This model is known as SEOBNRv4 in the LIGO Algorithm Library.

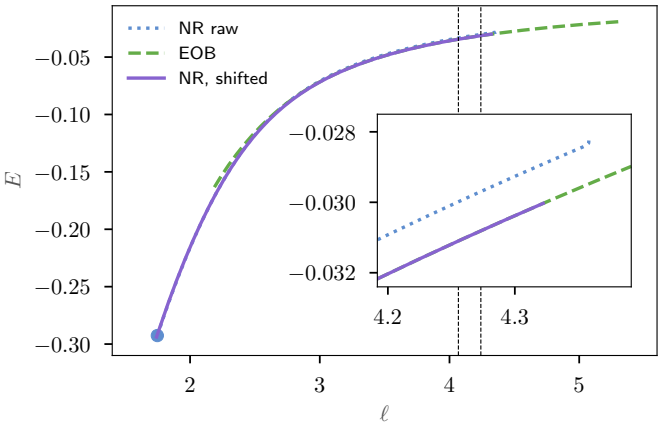

FIG. 2. The binding energy E as a function of the reduced orbital angular momentum ℓ for an equal mass binary with dimensionless spins $\chi_1 = \chi_2 = 0.6$. The dashed green curve corresponds to EOB data, while the dotted blue and solid purple curves are the raw and shifted NR data, respectively. The curves were aligned in the ℓ-interval $(4.07, 4.24)$ shown as dashed vertical lines. The dot indicates the state of the black hole as measured from quasi-local quantities. The inset highlights the requirement for the shifted NR curve in the early inspiral behavior (note that this shifted NR curve is also truncated to eliminate junk radiation).

i.e., that the binding energy of a spinning BBH configuration can be approximated by the *sum* of separate contributions, as predicted by PN theory (see e.g. [13]) and applied successfully for NR simulations of neutron stars [56–58]. When the spins are oriented only along the orbital angular momentum, the dependence of the individual contributions in Eq. (6) on the spin orientation can be given explicitly. Here, for equal-mass cases, the nonspinning point-mass term E_0 is independent of spin; the spin-orbit term $E_{SO} \propto (S_1 + S_2)$; the self-spin (S^2) term $E_{S^2} \propto S_1^2 + S_2^2$; the spin-spin (SS) interaction term $E_{SS} \propto S_1 S_2$; the cubical self-spin term $E_{S^3} \propto S_1^3 + S_2^3$ and lastly, the additional cubical spin term $E_{S^2S} \propto S_1^2 S_2 + S_1 S_2^2$. In PN theory, the different terms in Eq. (6) enter at different orders: SO terms start at 1.5 PN, spin-squared terms start at 2PN, and cubic-in-spin terms start at 3.5PN. Quartic-in-spin contributions are not included in this paper, but PN results have been presented in [59].

All individual contributions in Eq. (6) can be calculated by combining simulation with different spin orientations. The overall sign of the individual pieces and their magnitude depend on the spin magnitude, the spin's orientation, and the size/sign of the prefactor of every binding energy contribution.

D. Error estimates

The presented gauge invariant quantities have several possible uncertainties: truncation errors due to numeri-

cal discretization, errors due to finite radii extraction, filtering errors, and alignment errors. All uncertainties are included in our work and a detailed description is given below.

Numerical discretization: Every NR simulation is only an approximate representation of the continuum solution of the general relativistic field equations; thus, truncation errors ($\epsilon_{\rm trunc}$) affect all results. In general, SpEC shows small absolute errors for the waveforms phasing [41, 50, 60, 61]. Consequently, we expect the same for the binding energy, orbital angular momentum, and orbital frequency. To quantify the uncertainty caused by resolution effects, we perform our analysis for the same physical configuration using the two highest resolutions available. The truncation error is estimated as the difference between the resolutions. For most cases, the relative truncation error is typically of the order of 0.1% .

Finite radii extraction: Another possible source of error is caused by the finite radii extraction of the waves and the need for extrapolation of the waveform to infinity to eliminate near-field effects. In SpEC the extrapolation is done in the co-rotating frame [62], in terms of a corrected radial coordinate [63] using several extrapolation orders $N = 2, 3, 4$. It has been shown for many SpEC waveforms that GW extraction errors ($\epsilon_{\rm extrap}$) are comparable with truncation errors [64]. For the computation of the fluxes, which depend on the amplitude of the gravitational waves and their time derivates, extrapolation errors can be significant. In [65] it was found that higher-order extrapolation produces more accurate results in the inspiral but can amplify high frequency noise during merger-ringdown, leading to non-convergence, especially for subdominant modes. To avoid amplification of noise during merger, we choose not to use $N = 4$ waveforms in this work. Comparing $N = 2$ and $N = 3$ waveforms reveals that the latter is less sensitive to the effect of omitting data at small radii when performing extrapolation. Although $N = 3$ introduces more noise during ringdown, the effect on the binding energy curves is rather small. Thus, we adopt $N = 3$ for all the results in the paper. To estimate $\epsilon_{\rm extrap}$ we consider the difference in $E-\ell$ and $E-x$ curves between $N = 2$ and $N = 3$. For the majority of cases considered here, this gives a relative error of order 0.5%, which is approximately a factor of 5 larger than the truncation error and is the dominant source of uncertainty for most cases.

Aside from errors inherent to the NR waveforms themselves, other sources of error will enter the computation of $E - \ell$ and $E - x$ curves.

Alignment procedure: The alignment procedure, which is needed to compensate for the junk radiation, relies on the accuracy of the EOB approach and a properly chosen alignment window. We tested the effect of using different EOB approximants (the uncalibrated/calibrated SEOBNRv2 [28] and SEOBNRv4 [34] and the EOB model of [30]). While we found best agreement with [30], the effect was small. Hence, because of convenience, the calibrated SEOBNRv4 model is used throughout the paper. The effect of the alignment error ($\epsilon_{\rm al}$) is studied by: i) changing the alignment window from $[0.94, 0.98]\ell_{\rm max}$ to $[0.9, 0.98]\ell_{\rm max}$ and taking the difference between the results (ϵ_{int}) and ii) aligning to SEOBNRv2 instead of SEOBNRv4 and again taking the difference between the results ($\epsilon_{\rm v2}$). We find the relative errors to be of order 0.1% in $E - x$ and $E - \ell$ curves.

Filtering: For computation of $E - x$ curves, another possible source of error ($\epsilon_{\rm filt}$) is the use of a Savitzky-Golay filter for the computation of the PN parameter x. To gauge the impact of the chosen stencil size, we redid the computation using half as many points for filtering and taking the difference with the standard procedure. We find that these errors are on the order of 0.1% in $E - x$ curves.

We use the L_1 norm to combine the alignment errors and L_2 norm to compute the total error estimate:

$$\epsilon_{\rm al} = |\epsilon_{\rm v2}| + |\epsilon_{\rm int}|, \tag{7}$$

$$\epsilon_{\rm total} = \sqrt{\epsilon^2_{\rm al} + \epsilon^2_{\rm trunc} + \epsilon^2_{\rm extrap} + \epsilon^2_{\rm filt}}. \tag{8}$$

We compute this error estimate for every $E-j$ and $E-x$ curve, and use standard error propagation to compute errors in linear combinations giving the various contributions to the total binding energy. Where multiple resolutions are not available, the truncation error is taken to be the maximum error among all other configurations.

III. NON-SPINNING BINARIES

A. Imprint of the mass ratio

To isolate point-particle contributions from the binary dynamics, we start by considering non-spinning binaries. Figure 3 (top panel) shows the binding energy as a function of the reduced orbital angular momentum for a subset of simulations in Table II. There is a clear trend in the data: for higher mass ratios and for given value of ℓ, the system becomes more bound and merges at smaller values of ℓ. This observation is in agreement with PN predictions, once higher PN orders are included.

The opposite trend in mass ratio is demonstrated in the middle and bottom panel of Fig. 3, in which the binding energy and angular momentum as a function of the PN parameter x are presented. For a fixed value of x (i.e. orbital frequency), the most unequal binaries are the least bound and have the lowest values of angular momentum.

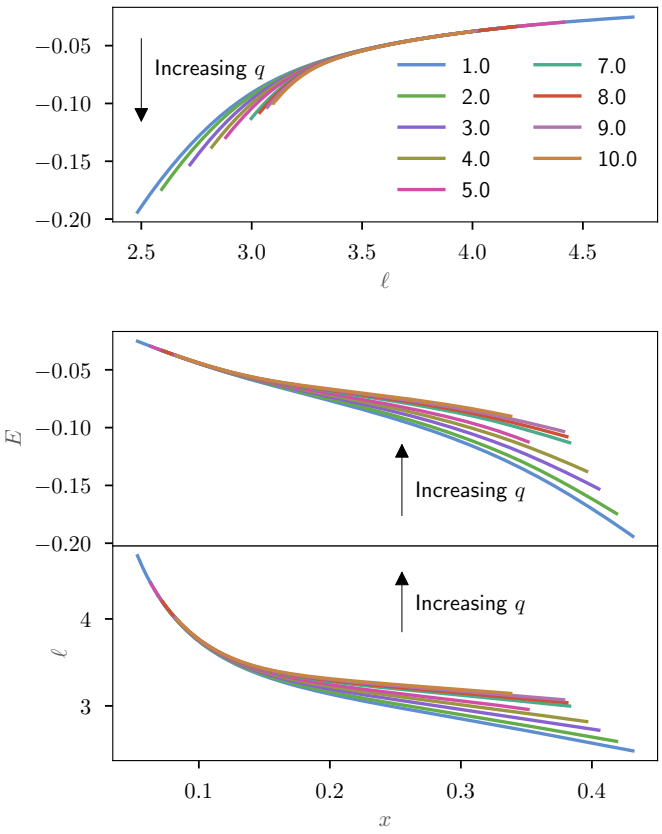

FIG. 3. Top panel: Binding energy E as a function of the reduced orbital angular momentum ℓ. Consistent with the Newtonian limit all $E(\ell)$ curves approach the same value for large ℓ. The curves show a hierarchy in which for fixed ℓ the most unequal mass systems are the most bound, where we define $q \geq 1$. Middle panel: Binding energy E as a function of x, where for a fixed x, higher mass ratio systems are less bound. Bottom panel: Reduced orbital angular momentum ℓ as a function of x. For fixed x the angular momentum increases for increasing q.

B. Comparison with waveform approximants

Next we compare the NR results to PN predictions, calibrated/uncalibrated EOB models [34][2], as well as the non-spinning NR surrogate from [8]. Previous comparisons between PN, EOB, and NR curves have been presented in e.g. [30, 35, 66].

Unsurprisingly, the PN predictions show the largest difference with NR data as seen in the top left panel of Figure 4. The error grows quickly as a function of x, where equal mass systems show the largest fractional error. It should be noted, however, that during the inspiral the error is still small $\lesssim 6\%$ until $x = 0.2$ which is close to merger. The top right panel shows the difference with the uncalibrated SEOBNR model. The difference with NR data is smaller and the agreement persists to higher frequencies showcasing the effect of the EOB approach. In the bottom left panel, the difference with respect to the full calibrated model (SEOBNR) is shown. Here, the differences are even smaller, which indicates that the calibration of the model to match NR waveforms also improves the agreement of the conservative dynamics. Finally, the bottom right panel contrasts the NR data with a surrogate model. We find the smallest differences here, as expected from a model that is entirely based on NR information. Although the surrogate provides a very powerful way to obtain NR information (dynamics and waveforms), it is limited in scope of application in two crucial ways: i) the information is only available about the last $\simeq 15$ orbits prior to merger, and ii) the results are only accurate inside the domain where the surrogate is constructed (i.e. $1 \leq q \leq 10$).

C. Phenomenological $E(x)$ - fit

Generically, $E(x)$ depends sensitively on the symmetric mass ratio $\nu = \mu/M$. An examination of the 4PN expression for the binding energy [67] shows that progressively higher powers of ν appear at each PN order. Schematically, the expansion is

$$E(x) = -\frac{x}{2}(1 + c_1 x + c_2 x^2 + c_3 x^3 + c_4 x^4), \qquad (9)$$

where the coefficients c_i are polynomial functions of ν. Starting at 4PN, terms logarithmic in x also appear. We construct a fit for the binding energy using the following procedure. First we introduce unknown higher order coefficients c_5, $c_{5\log}$, c_{55} corresponding to the 5PN non-log and log corrections and the 5.5 PN correction, respectively. We then consider a log-resummed expression for the binding energy

$$E(x) = -\frac{x}{2}\left(1 + \log[1 + a_1 x + a_2 x^2 + a_3 x^3 + a_4 x^4 + a_5 x^5 + a_{55} x^{11/2}]\right) \qquad (10)$$

following [22]. The coefficients a_i for $i = 1, ..., 4$ are completely constrained by post-Newtonian theory, while c_5 and $c_{5\log}$ enter a_5 and trivially $a_{55} = c_{55}$. We fit this log-resummed expression separately to each dataset for all the different mass ratios. Then we fit each coefficient to a low order polynomial in the symmetric mass ratio. This allows us to assemble the full mass ratio dependence of $E(x)$. The coefficients are:

[2] The uncalibrated model is obtained from SOEBNRv4 by setting all calibration and NQC parameters to zero.

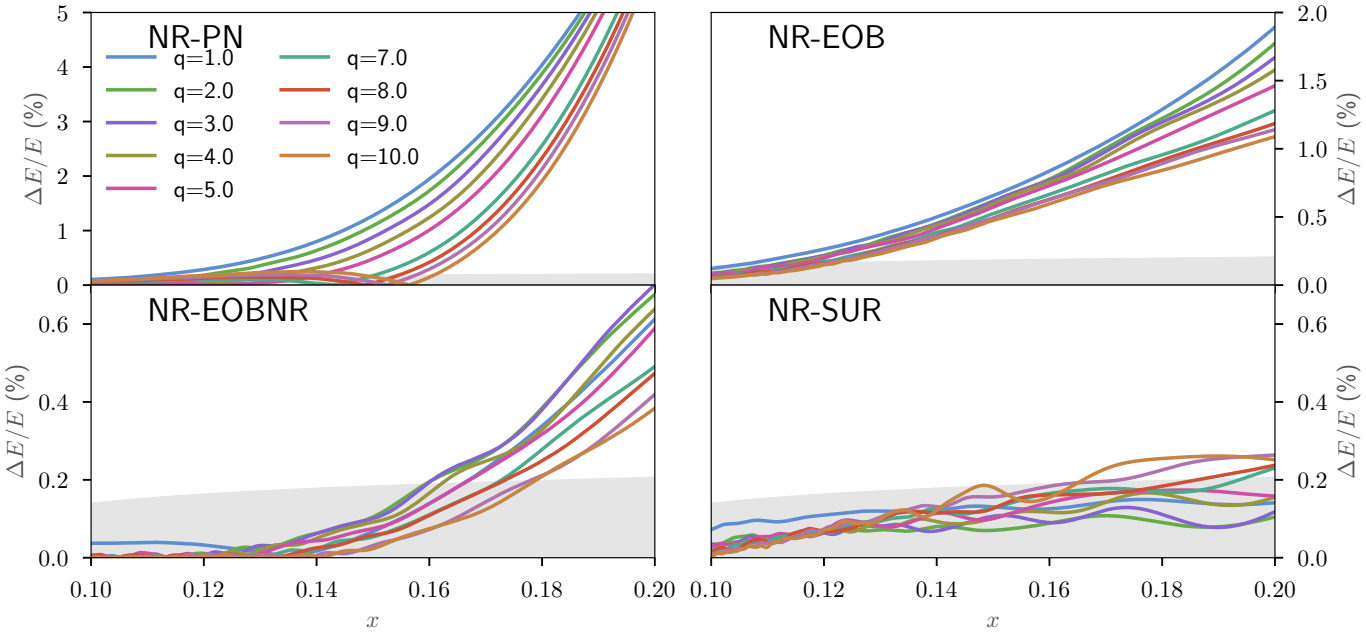

FIG. 4. Difference of NR binding energy $E(x)$ with respect to PN (upper left panel), uncalibrated EOB (upper right panel), calibrated EOBNR (lower left panel), and the non-spinning surrogate [8] (lower right panel). The gray region represents an estimate of the NR error, given as the maximum of all errors in all the curves. Notice the improvement in the agreement of the calibrated EOBNR model compared to the uncalibrated EOB model.

$$c_5 = -605.96 + 20901\nu - 76662\nu^2 + 84623\nu^3 \quad (11)$$

$$c_{5log} = 454.06 + 14360\nu - 60400.0\nu^2 + 56875\nu^3 \quad (12)$$

$$c_{55} = 1271.2 - 81986\nu + 320930\nu^2 - 327270\nu^3 \quad (13)$$

Figure 5 demonstrates the excellent agreement of the fit with the original data, giving even slightly better performance than the NR surrogate. We also test the fit by comparing it with NR data that were not used for construction. These curves are shown as bold, dashed-dotted lines in Figure 5. As one can see, the agreement remains remarkable up to the very late inspiral. We note that the fit is only applicable in the region $x \leq 0.2$ and nominally limited in the range of mass ratios to $q \in [1, 10]$. However, we have verified that reasonable results are even obtained outside of this range, e.g. for $q = 100$, by comparing results to SEOBNR predictions.

There are several possible applications for the phenomenological fit obtained with Eq. (10). While it is obvious that the fit can be used to directly test the dynamics inferred from waveform models, it might also be used to constrain higher order PN terms, see e.g. [68]. Additionally, an alternative calibration of the EOB A-potential is possible. Restricting to circular orbits, i.e., to a vanishing radial conjugate momentum, one can compare Eq. (10) with $E = (H_{\rm EOB} - M)/\mu$ and obtain the EOB-Hamiltonian $H_{\rm EOB}$ and thus the unknown high order PN coefficients in the A-potential. This allows a direct calibration of the conservative dynamics of EOB without the direct use of the waveform.

Name	(00)	(↑ 0)	(↓ 0)	(↑↓)	(↑↑)	($\frac{1}{2}$0)
SXS ID	0180	0227	0585	0217	0152	0223
χ_1	0.0	0.6	-0.6	0.6	0.6	0.3
χ_2	0.0	0.0	0.0	-0.6	0.6	0.0

TABLE I. Configurations used to separate out contributions to the binding energy.

IV. EQUAL MASS, ALIGNED SPIN BINARIES

A. Extracting spin contributions

As a starting point for extracting spin-dependent contributions to the binding energy, we begin by considering a sequence of equal-mass, non-precessing simulations. By neglecting quartic-in-spin corrections, all the individual components identified in Eq. (6) can be extracted from the simulations in Table I using the following linear com-

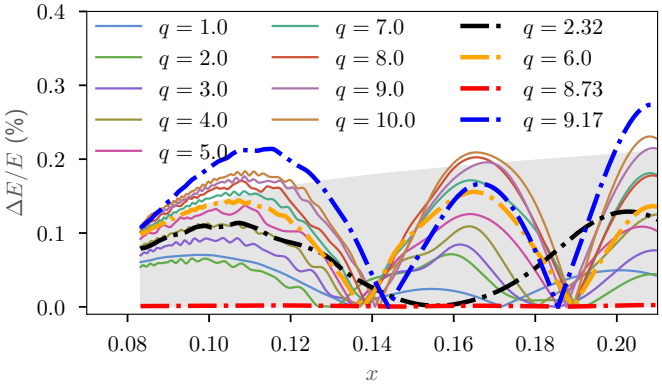

FIG. 5. The difference between the binding energy of our NR data and the phenomenological fit, Eq. (10). The thin solid lines correspond to the same curves shown in Figure 4. The dashed-dotted lines showcase the agreement with configurations that were *not* used in the construction of the fit. All differences are essentially within the NR error estimate, shown in gray.

binations (see also [56, 57]):

$$E_{SO} = \frac{1}{6}\left[-(\downarrow 0) + 16\left(\frac{\uparrow}{2}0\right) - 12(00) - 3(\uparrow 0)\right], \quad (14)$$

$$E_{S^2} = \frac{1}{2}\left[(\downarrow 0) - 2(00) + (\uparrow 0)\right], \quad (15)$$

$$E_{SS} = (\downarrow 0) - (00) - (\uparrow\downarrow) + (\uparrow 0), \quad (16)$$

$$E_{S^3} = \frac{1}{3}\left[-(\downarrow 0) - 8\left(\frac{\uparrow}{2}0\right) + 6(00) + 3(\uparrow 0)\right], \quad (17)$$

$$E_{S^2S} = \frac{1}{2}\left[-(\downarrow 0) + 2(00) + (\uparrow\downarrow) - 3(\uparrow 0) + (\uparrow\uparrow)\right]. \quad (18)$$

Figure 6 shows the $E-\ell$ and $E-x$ curves for all configurations after applying the procedure described in Sec. II B. Furthermore, it shows clearly that the larger the total angular momentum of the binary, the higher the frequency of merger and the lower the orbital angular momentum. This effect is sometimes referred to as the hang-up effect [69]. We further find that the curves corresponding to the non-spinning (00) configuration and to the $(\uparrow\downarrow)$ configuration lie essentially on top of each other, since the leading order difference is the quadratic-in-spin term.

Using Eqs.(14)-(18) we obtain the various contributions shown in Fig. 7. The right panels highlight the linear, quadratic and cubic-in-spin terms. Throughout the inspiral, the spin-orbit term dominates the others by an order of magnitude. On the other hand, the quadratic and cubic-in-spin terms have comparable magnitudes, with the quadratic terms growing larger near the merger.

To evaluate how well the energy components are extracted and to test our ansatz, Eq. (6), we check whether we can reconstruct the full $E-x$ curves for simulations which were not used in the computation above. In particular, we choose six equal-spin cases and six unequal spin cases, as described in Table III. The $E-x$ curves are reconstructed as

$$E = E_0 + E_{SO}\frac{\chi_1}{\chi_0} + E_{SO}\frac{\chi_2}{\chi_0} + E_{S^2}\frac{\chi_1^2}{\chi_0^2} + E_{S^2}\frac{\chi_2^2}{\chi_0^2} + E_{SS}\frac{\chi_1\chi_2}{\chi_0^2}, \quad (19)$$

where $\chi_0 = 0.6$. Note that we omit the cubic-in-spin terms as they are not measured with sufficient accuracy. A detailed analysis of the case $\chi_1 = -0.4$, $\chi_2 = 0.8$ is shown in Fig. 8, in which we also include SEOBNR results [34] for comparison. Early in the inspiral, both the EOB approximant and the NR reconstructed curves stay close to the NR data. As the frequency increases, the EOB approximant departs from the NR curve, while the reconstructed curve remains close throughout the inspiral, although it leaves the region of NR error near merger. The behavior presented in Fig. 8 is typical for the cases we have considered. In Fig. 9, we present the residuals between NR, EOB and the reconstructed results. For unequal spins, the difference between the reconstructed curves and NR result remains small throughout the inspiral (typically below 0.3%) and throughout the entire simulation $\lesssim 3\%$. Only for the two extreme cases with $\chi_1 = \chi_2 = \pm 0.97$, the curves show more disagreement $\lesssim 0.7\%$ during the inspiral and around merger $\simeq 6\%$. The larger disagreement for higher spin magnitudes indicates the importance of cubic-in-spin contributions.

The calibrated EOB models also perform well, with errors below 0.5% during the early inspiral and maximum errors throughout the simulation $\lesssim 10\%$.

Having extracted the various components of energy, we proceed to a detailed comparison with different models.

B. Comparison with waveform approximants

1. *Spin-orbit effects*

We begin by considering the spin-orbit effects, which enter at 1.5 PN order. In the left panel of Fig. 10, we compare NR data to PN expression for the spin-orbit contributions to the binding energy up to 3.5 PN order, as well as to predictions from EOB with (SEOBNR) and without NR calibration and the NR surrogate model [9]. Early in the inspiral, the agreement between NR and PN (and all other models) is very good, with differences of about 1%. However, as the inspiral proceeds, the PN curves deviate sharply from NR data, while the other curves continue to track the NR data much longer. The surrogate has the smallest differences but once more suffers from length and parameter space constraints that limit its application. Considering the difference between the uncalibrated EOB model and SEOBNR, we find that during most of the inspiral ($x \lesssim 0.2$), the calibrated model performs better than the uncalibrated one, with the uncalibrated models doing slightly better closer to merger.

The effect of PN order is shown in the right panel of Fig. 10. For the early inspiral, increasing the PN order

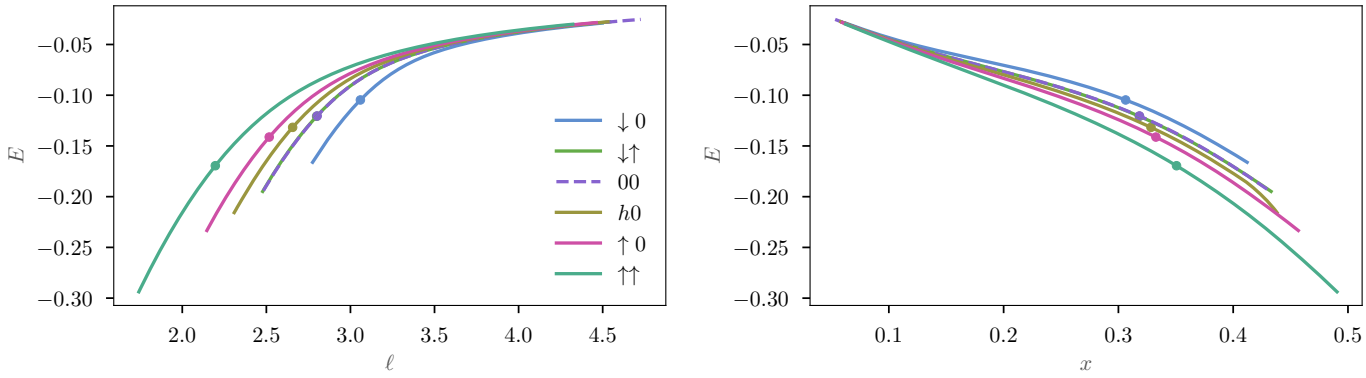

FIG. 6. The binding energy E as a function of reduced orbital angular momentum ℓ (left) and the post-Newtonian parameter x (right) for configurations from Table I. The scatter points indicate the location of the merger.

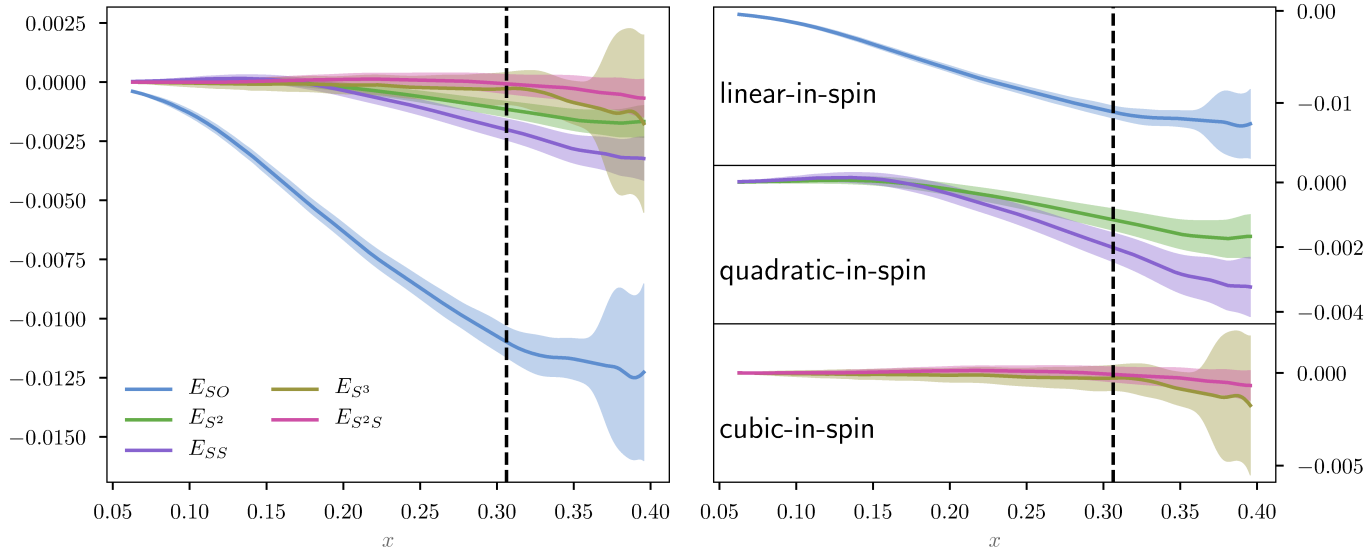

FIG. 7. Spin contributions to the binding energy as a function of x. The dashed vertical line represents the point of merger for the configuration that merges earliest (i.e., at the lowest frequency). The shaded regions represent the NR error. Note that the spin-orbit contribution is about one order of magnitude larger than the other spin contributions. The spin-squared and spin-cubed terms are consistent with zero early in the inspiral and are monotonically decreasing as one approaches merger.

helps to capture better the NR data, however the 2.5 PN results are marginally better than the 3.5 PN. Once again, when the evolution approaches several orbits before the merger, the differences rise sharply.

2. *Spin-squared effects*

The results for the spin-spin term are shown in Fig. 11 and exhibit an interesting effect: during most of the inspiral, the PN and and NR curves agree, but after about $x \approx 0.12$ the SS contribution to the binding energy decreases, in contrast to the PN prediction which continues to grow monotonically. Meanwhile, using the same expression as for NR but with the surrogate and the EOB models, we reproduce the NR behavior. More pronounced than for the spin-orbit contribution, we find a smaller difference between the NR result and the uncalibrated EOB model than to the calibrated SEOBNR model. This shows that the calibration of the SEOBNR model, which focuses on minimizing unfaithfulness and difference in the time to merger [34], can result in a worse description of some aspects of the conservative dynamics in the strong field regime. One possible reason might be that the calibration parameters, which were introduced in the SEOBNR model, correspond to coefficients of higher unknown PN orders. When modeled as polynomials in ν, χ, these parameters break the symmetry underlying the extraction of the terms presented here.

Considering the effect of PN order, we find no difference in the behavior of the different PN expressions. All PN orders show a monotonic growth with x in contrast to NR and EOB, and virtually no improvement with increasing PN order is found. Exactly the same effects are

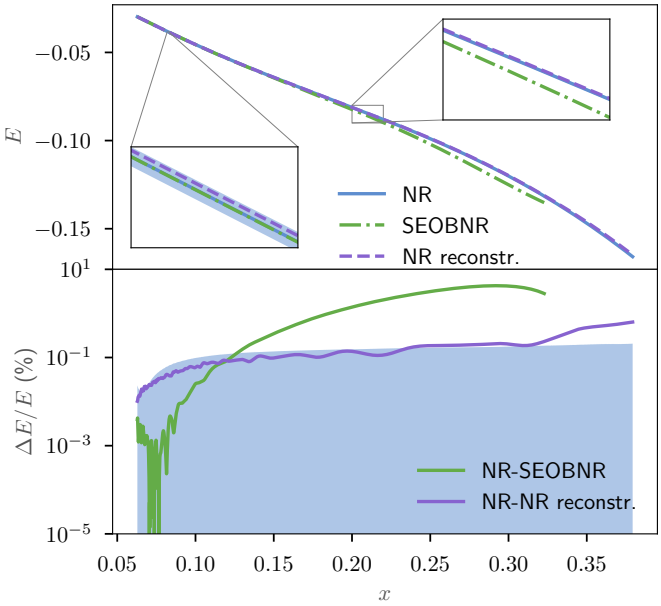

FIG. 8. Detailed analysis of the equal mass $\chi_1 = -0.4$, $\chi_2 = 0.8$ system. The top panel shows the binding energy while the bottom shows the fractional error. The NR error is shown as the shaded region.

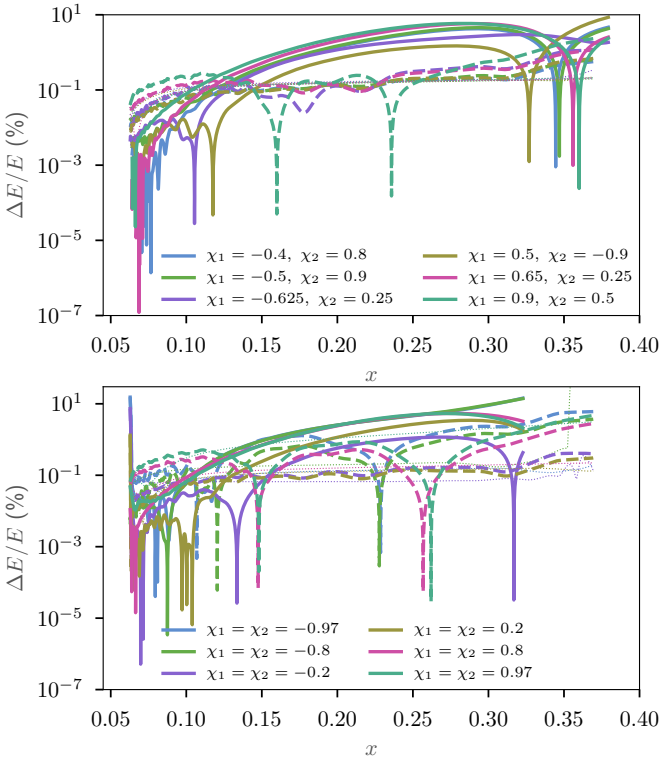

FIG. 9. Top panel: residuals of all the unequal spin cases from Table III between NR and SEOBNR (solid), NR and reconstructed (dashed). Bottom panel: same, but for equal spin cases. Both models show low residuals in the early inspiral, and the reconstructed curves generally have smaller residuals at higher frequencies and stay within the NR errors (indicated by dotted curves) longer.

present in the self-spin contribution, with the only difference being that the magnitude of the self-spin effect is slightly smaller.

3. *Cubic-spin effects*

Finally we consider cubic-in-spin contributions to the binding energy. To enhance the effect we consider the combination of both types, namely $E_{S^3} + E_{S^2S}$. Figure 12 shows the results. The spin-cubed effects from the NR data display residual oscillations due to eccentricity and are relatively noisy. For this reason, for cubic-in-spin terms we focus on the qualitative behavior and put an upper bound on them. For most of the inspiral, all the models except the calibrated EOB stay within the NR error. This is likely due to the symmetry breaking terms mentioned earlier. It should be noted, however, that these effects are small and contribute little to the overall disagreement. We leave it to future work to explore the cubic-in-spin terms in more detail with the aid of additional NR simulations.

V. GENERIC SPIN ALIGNED BBHS

In this section we extend our investigation to aligned-spin binaries with various masses ratios and spin magnitudes. We compare the obtained binding energies with state-of-the-art waveform approximants and present a method to phenomenologically describe generic spin-aligned systems.

A. Comparison with waveform approximants

1. *Total binding energy*

In the following we construct the $E - x$ curves for a set of 70 simulations of unequal mass, non-precessing binaries described in Table IV and compare those to PN and SEOBNR predictions. The PN curves include non-spinning terms up to 4PN order, spin-orbit terms up to 3.5 PN order, spin-spin terms up to 4PN order, and cubic-in-spin terms up to 3.5 PN order. Figure 13 shows the difference between NR, SEOBNR and PN curves separately for mass ratios $q = 2$ (left panels) and $q = 3$ (right panels). The top panels show all considered $E(x)$ curves for the given mass ratios. In the inspiral ($x \lesssim 0.1$) both PN and SEOBNR agree with NR remarkably well, with errors of order 0.1%. Closer to merger, the PN errors grow quickly to about $\sim 10\%$ and are consequently several times larger than EOB errors, which are typi-

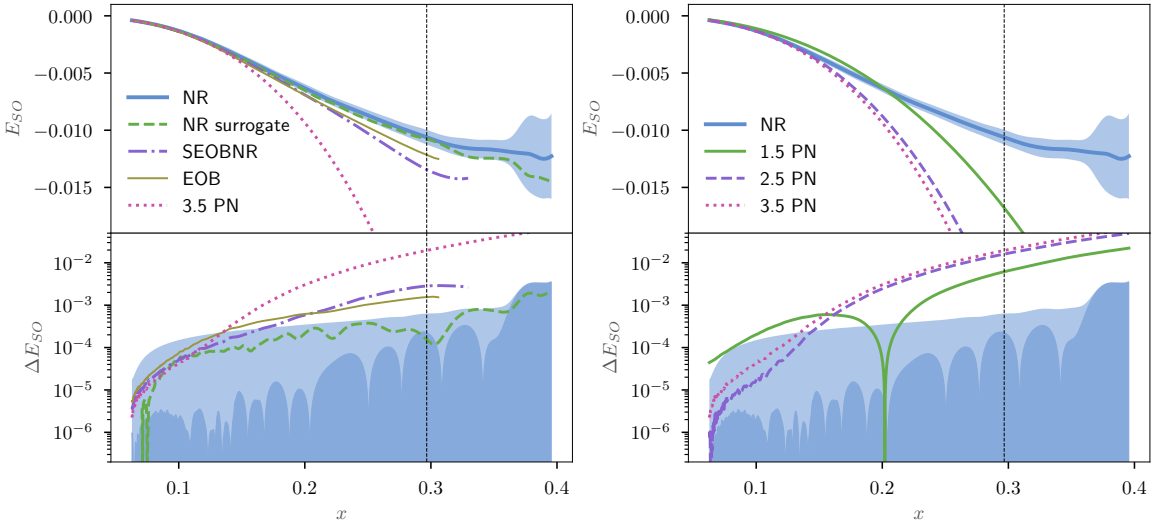

FIG. 10. Left: the spin-orbit contribution to the binding energy E as a function of x from NR (blue thick), the NR surrogate (dashed), SEOBNR (dashed-dotted), EOB (thin) as well as the PN result up to 3.5 PN order (dotted). Note the good agreement of PN in the inspiral, which quickly deteriorates at $x \approx 0.12$ where the binary is only a few orbits to merger. The surrogate and EOB curves track the NR results substantially longer. The EOB curves terminate at EOB merger. The bottom panel shows the residuals between the approximants and NR. Until late inspiral, the surrogate and SEOBNR remain within the NR error. The light shaded region gives the estimate of NR error as defined in Sec. II D. The dark shaded region shows instead the difference in the result between two different NR resolutions, a common metric used in literature. It is evident that our error estimate is indeed conservative. Right: comparison of binding energy in NR and PN at various orders. Throughout the inspiral, the results with at 2.5 PN order are closest to NR. The dashed vertical line indicates the merger of the NR simulation that merges at the lowest frequency ($\chi_1 = \chi_2 = -0.6$).

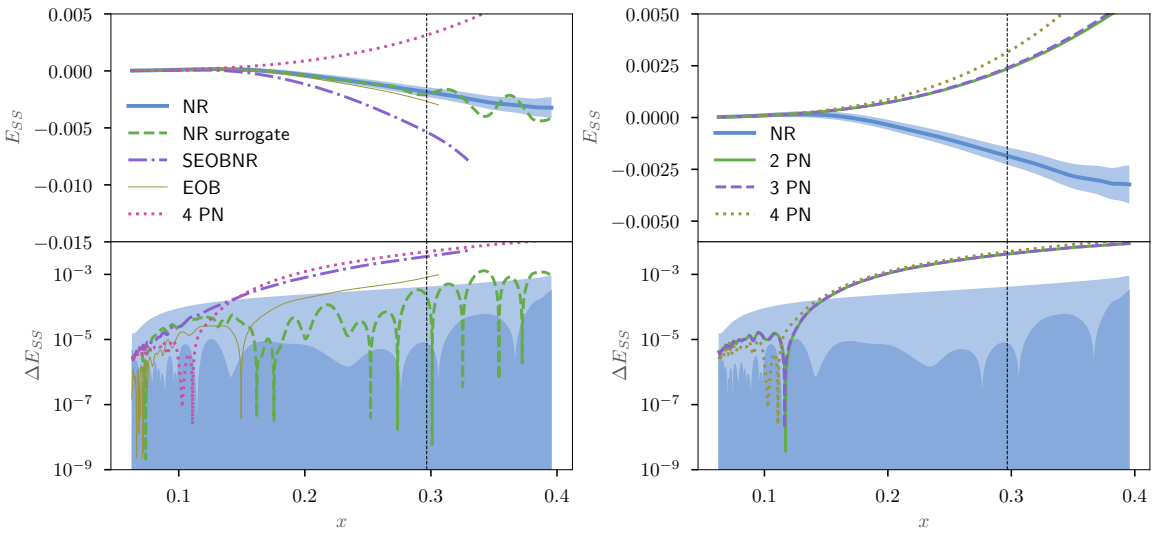

FIG. 11. As Fig. 10 but showing the spin-spin interaction. Left: the spin-spin contribution to the binding energy E as a function of x from NR, PN expression up to 4 PN order as well as SEOBNR, EOB and surrogate. Note the sharp contrast of the behavior between PN and the other models close to merger: the PN prediction grows monotonically, while the rest decrease.

cally $\sim 1\%$. The bottom panels show the error for both SEOBNR (left) and PN (right) at $x = 0.2$ as functions of the two spins. From the PN results, one notes that for cases with large negative spins on the primary black hole, the error is larger. This pattern is explained by considering contours of the effective spin, shown as labeled gray lines: the error is smallest for large positive $\chi_{\rm eff}$ and grows monotonically as the effective spin decreases. This is another manifestation of the hang-up effect: cases with larger $\chi_{\rm eff}$ merge at higher frequencies than those with large negative effective spins. Since we are computing the error at a fixed frequency, for some cases it is evaluated "closer" to merger than for others. In contrast, such a correlation is not present for the SEOBNR model which

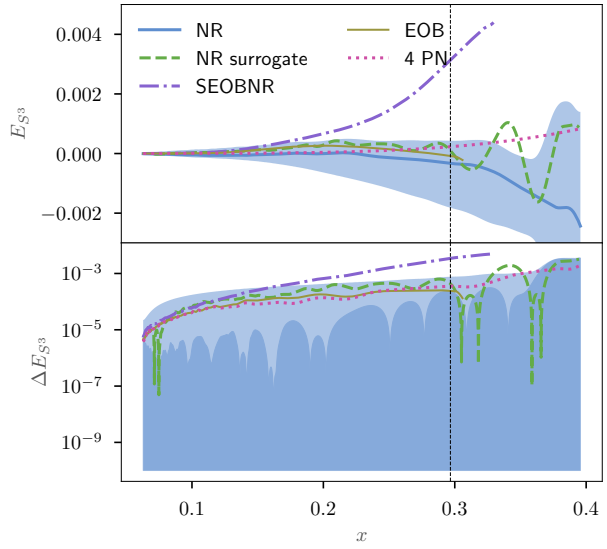

FIG. 12. The cubic-in-spin contribution to the binding energy E as a function of x from NR, PN as SEOBNR, EOB and surrogate. Since the uncertainties in the NR results are large, we are in effect putting an upper bound on the cubic terms. Note the sharp contrast of the behavior between calibrated EOB versus the other models. We do not show a comparison between various PN orders since spin-cubed terms are only known to leading order.

shows small errors for all values of the effective spin. The same picture applies to the $q = 3$ case, with the main difference being the larger values of error at fixed frequency, as seen in the right panel of Fig. 13.

Considering cases with $q \in (5, 7, 8)$, we find qualitative agreement with results with lower mass ratios. For a given effective spin, the cases with higher mass ratios have higher errors for PN, while the errors are essentially unchanged for SEOBNR.

When repeating this procedure using the SEOBNRv2 models we find that for different cases one model may have lower errors than the other, but no distinct pattern emerges. This is because SEOBNRv4 was constructed to attain better unfaithfulness with NR in a larger region of parameter space, and includes no direct information about the binding energy.

2. *Spin-orbit contribution*

After comparison of the total energies, we proceed to extract the various energy components for the cases where this is possible as described in Appendix A. The top panel of Figure 14 demonstrates the typical behavior of the spin-orbit term for a $q = 8, \chi_1 = 0.5, \chi_2 = 0$ system, the bottom panel shows the same behavior for all other cases. At low frequency both models agree well, but as the inspiral proceeds, the SEOBNR model has differences smaller by an order of magnitude.

The *absolute* errors in the spin-orbit term for SEOBNR and PN are shown in bottom panels of Fig. 14 for the $q = 8, \chi_1 = 0.5, \chi_2 = 0$ system as well as all cases. At low frequency the errors are $\sim 10^{-5}$ for both models, corresponding to fractional errors of $\sim 1\%$. As the frequency increases, the errors grow faster in PN than SEOBNR, such that in the late inspiral the SEOBNR fractional errors are $\sim 8\%$, a factor of 5 smaller than PN.

Previously we saw that for an equal-mass binary we were able to rescale the spin-orbit contribution to the energy from a given configuration to one with different spins, simply by rescaling by the magnitude of the spin. It is interesting to examine whether the various definitions of effective spins proposed in the literature can serve the same task. To do so we rescale all the NR results by different effective spins and compute the *coefficient of variation*, $CV \equiv \frac{\sigma}{\mu}$ where μ and σ are the mean and standard deviations respectively. We use the following definitions:

$$\chi_{\rm mw} = \frac{m_1\chi_1 + m_2\chi_2}{m_1 + m_2}, \tag{20}$$

$$\chi_\phi = \chi_{\rm mw} - \frac{38\nu}{133}(\chi_1 + \chi_2), \tag{21}$$

$$\chi_{H_{SO}} = \nu\left[\left(\frac{3}{4} + \frac{m_1}{m_2}\right)\chi_1 + \left(\frac{3}{4} + \frac{m_2}{m_1}\right)\chi_2\right]. \tag{22}$$

Surprisingly, Figure 15 shows that it is the effective spin that corresponds to the phase evolution χ_ϕ results in the smallest overall spread, followed by the Hamiltonian inspired spin $\chi_{H_{SO}}$ and the standard mass-weighted spin $\chi_{\rm mw}$. Thus, χ_ϕ should be used when trying to reduce dimensionality of the problem.

3. *Spin-squared contribution*

We finish the binding energy comparison by considering the spin-squared contributions. As before, the generic behavior we saw for equal masses carries over to this case: PN generically predicts a monotonic spin-squared contribution, while SEOBNR correctly follows the NR results that have a local maximum, as shown in Fig. 16. The absolute errors for all cases are summarized in the bottom panel of Fig. 16 and show a similar behavior as the spin-orbit contribution. In the early inspiral, the errors are of order 10^{-5}, which corresponds to a fractional error of $\sim 10\%$. However, they increase very quickly with PN errors growing faster than EOB errors.

B. Phenomenological E-x curves

Next we investigate if we can extend the phenomenological discussion of the binding energy for non-spinning

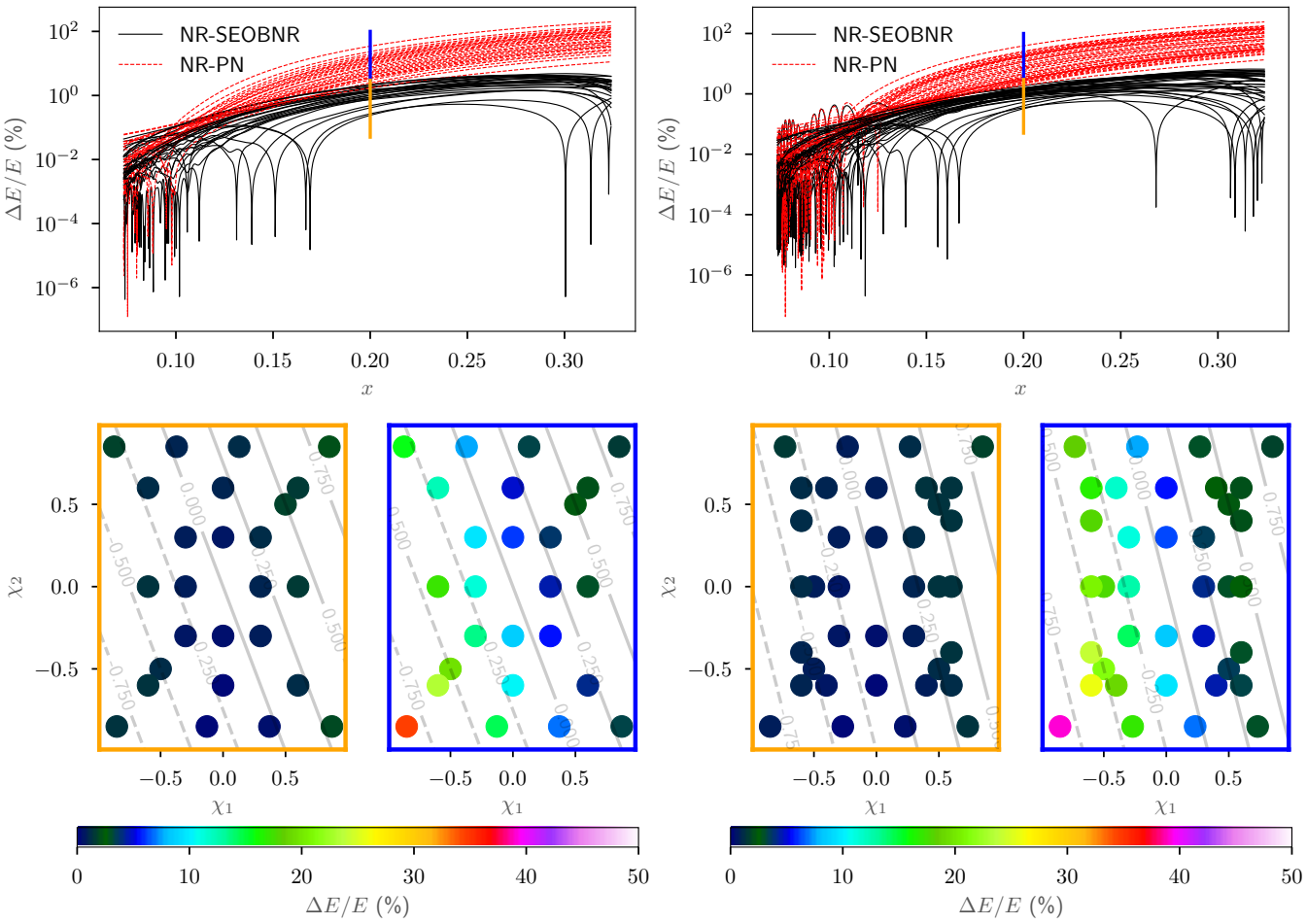

FIG. 13. Fractional differences between NR, SEOBNR (black) and PN (red, dashed) $E - x$ curves for $q = 2$ (left) and $q = 3$ (right). The top panels give an overview demonstrating the errors as a function of frequency. Note the excellent agreement of PN and SEOBNR with NR in the early inspiral. The bottom panels show the differences evaluated at $x = 0.2$ as functions of the two aligned-spin components for SEOBNR (left) and PN (right). In gray are contours of constant χ_{eff}, with negative values dashed.

and equal mass aligned-spin cases, with the aim of finding a closed-form expression for binding energy contributions for generic spin-aligned systems. Assuming that the *form* of the binding energy in NR is similar to that in PN theory, the spin-orbit contribution can be expressed as

$$E_{SO} = x^{5/2}\nu\left[(S_1 + S_2)A(\nu, x) + (S_1/q + qS_2)B(\nu, x)\right]. \tag{23}$$

Assuming that, for any fixed mass ratio the functions A, B are independent of spin, then given any two configurations $E_{SO}, \tilde{E}_{SO}$ with given mass ratio and spins that are not multiples of each other, one can trivially obtain A, B as functions of x. After fitting these functions for different mass ratios the spin-orbit term for all mass ratios and spins is determined. In principle, spin-squared coefficients may be extracted using the same approach; however, this is hampered by numerical uncertainties.

The accuracy of determining A, B depends on the accuracy of extraction of the spin-orbit terms, both in terms of numerical error and the contribution of higher spin terms. As proof of principle, we applied this approach using SEOBNR data as the underlying model for a set of 15 configurations between mass ratios 1.1−50 and using spin magnitudes of 0.6. We find the differences between the reconstructed curves and the EOB data from Tables III and IV, which were not used for the fit, to be $\lesssim 10^{-3}$ at $x = 0.3$, comparable to the expected magnitude contribution of the cubic-in-spin terms. This difficulty can in principle be overcome by creating data at more spin configurations to completely decouple the linear and cubic-in-spin terms. For SEOBNR this is feasible, but would require 10 configurations per mass ratio and thus is too computationally expensive for full NR simulations. Furthermore, combining an increasing number of datasets leads to a growth of uncertainty caused by the individual errors of the configurations.

Instead, we adopt a completely phenomenological

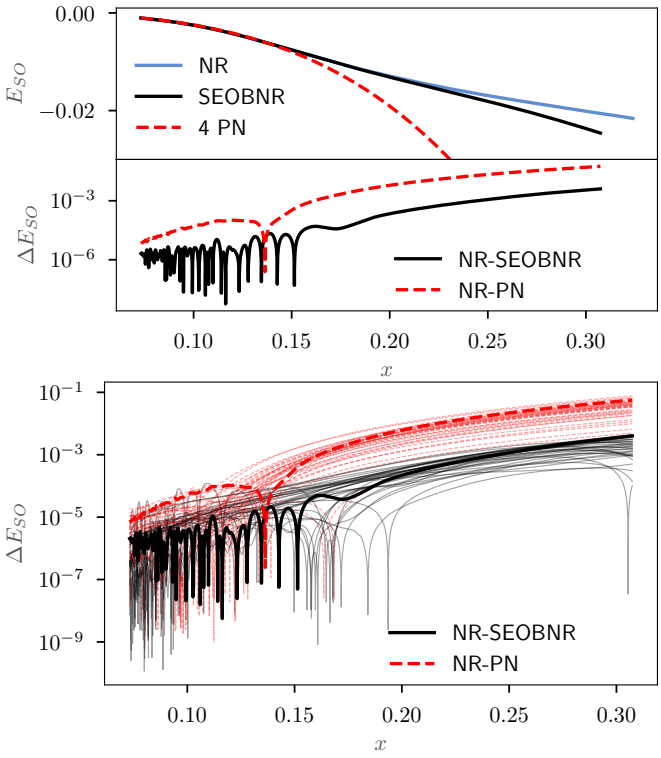

FIG. 14. Absolute differences between NR, SEOBNR (black, solid) and NR, PN (red, dashed) for the spin-orbit contribution. The top panel shows detailed behavior for the $q = 8.0, \chi_1 = 0.5, \chi_2 = 0$ case and the bottom shows all cases. Note that SEOBNR has fractional errors $\lesssim 8\%$ even in late inspiral ($x = 0.2$), while PN differences are a factor of 5 larger.

model for the odd-spin terms. In particular, we take

$$E_{SO} \approx \left(1 + \frac{a_3 x^3 + a_4 x^4 + a_5 x^5}{1 + b_1 x + b_2 x^2}\right) E_{SO}^{PN} \tag{24}$$

where E_{SO}^{PN} is 3.5PN expression, and a_i, b_i are polynomial functions of the symmetric mass ratio ν and the effective spin χ_ϕ. The particular form of Eq. (24) enforces that at small frequencies the PN prediction is obtained and correction only enter higher order PN terms. Furthermore, to preserve the correct symmetry under the transformation $(\chi_1, \chi_2) \to (-\chi_1, -\chi_2)$ the polynomials a_i, b_i are restricted to the form

$$p + s_0 \chi_\phi^2 + s_1 \chi_\phi^4 + n_0 \nu. \tag{25}$$

The fit is done in two steps: first, each E_{SO} curve is fitted to Eq. (24) and then all coefficients are fitted across parameter space. To ensure a good interpolation across parameter space, we use L_2 regularization with the regularization parameter of 1×10^{-6} (we exclude cases with $\chi_{\rm mw} < 0.15$ since the SO component is not as well determined as for the other cases). The results are summarized in Figure 17 which shows the same data as in Figure 14 except that it includes equal-mass, equal-spin

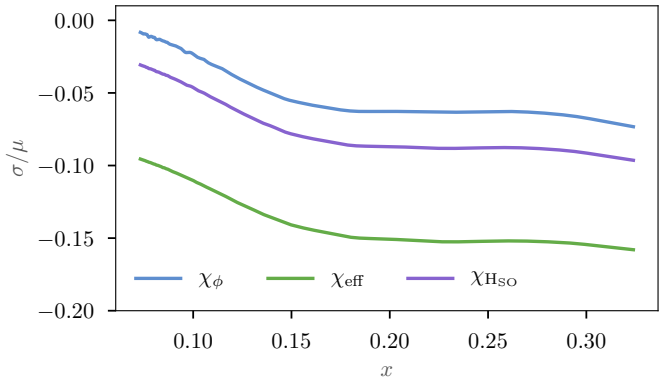

FIG. 15. The coefficient of variation as a function of x computed from all 35 (70) cases that we possess with (without) symmetry. It is clear that the effective spin that arises in phase evolution, χ_ϕ has the smallest spread.

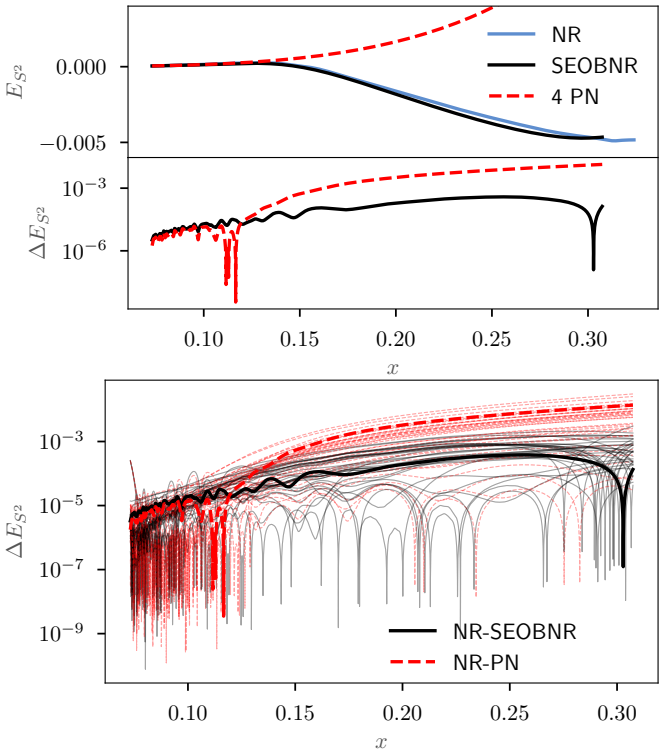

FIG. 16. Absolute differences between NR, SEOBNR (black, solid) and NR, PN (red, dashed) for the spin-squared contribution. The top panel shows detailed behavior for the $q = 8.0, \chi_1 = 0.5, \chi_2 = 0$ case and the bottom shows all cases. Note that SEOBNR has fractional errors $\lesssim 20\%$ even in late inspiral ($x = 0.2$), while PN no longer represents the contribution even qualitatively.

cases from Table III. Figure 17 shows that in the early inspiral the phenomenological curves show excellent agreement, comparable with SEOBNR. The error increases with frequency; in the late inspiral ($x = 0.3$) it reaches $\sim 4 \times 10^{-4}$, about a factor 8-10 smaller than SEOBNR.

The coefficients for the spin orbit terms are given by

$$a_3 = -37.684 - 35.577\chi_\phi^2 + 14.793\chi_\phi^4 + 136.37\nu \tag{26}$$
$$a_4 = 267.96 + 437.71\chi_\phi^2 - 199.08\chi_\phi^4 - 821.08\nu \tag{27}$$
$$a_5 = -271.96 - 722.11\chi_\phi^2 + 392.16\chi_\phi^4 + 1208.6\nu \tag{28}$$
$$b_1 = -10.404 - 0.52252\chi_\phi^2 - 1.9139\chi_\phi^4 + 3.9269\nu \tag{29}$$
$$b_2 = 30.308 + 15.715\chi_\phi^2 + 2.7542\chi_\phi^4 - 6.7698\nu \tag{30}$$

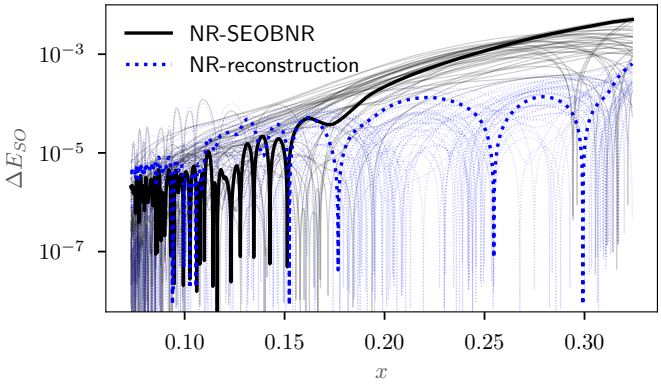

FIG. 17. Absolute differences NR and reconstruction (blue, dotted) for the spin-orbit contribution. For comparison the difference between NR and SEOBNR is shown in black thin lines. The thick curves correspond to the configuration $q = 8$, $\chi_1 = 0.5$, $\chi_2 = 0$. Early in the inspiral both curves have low errors, with SEOBNR errors being lower due to the alignment of the NR data to EOB waveforms as discussed in Sec. II B. As the inspiral proceeds, the error in the reconstructed curves remains lower, staying below 4×10^{-4} for $x \approx 0.3$.

VI. SUMMARY AND CONCLUSION

In this article, we presented a detailed study of the energetics of aligned-spin binary black hole systems. This allows direct testing of the conservative dynamics in the strong field regime, see e.g. [30, 35, 66].

We discussed in detail how the ambiguous offset caused by the initial burst of junk radiation can be removed and studied in great detail possible numerical errors/uncertainties. Based on the constructed curves, we compared results obtained from numerical relativity simulations with PN [13] and EOB approximants [28, 30, 34], as well as for the non-spinning case with an NR surrogate model [8]. We find overall a very good performance of EOB approximants as well as for the surrogate model, while the PN approximant is not capable of predicting the conservative dynamics accurately within the last orbits before merger.

For the non-spinning binaries, the obtained fractional differences between the NR data and the considered EOB approximants (SEOBNR) is $\approx 0.2\%$ during the inspiral and $\approx 1\%$ at merger. The NR surrogate achieves fractional errors always on the order of the NR uncertainty; i.e., $\approx 0.2\%$. In addition to these comparisons, we presented a phenomenological fit to non-spinning systems with mass ratios up to $q = 10$ allowing an accurate representation of the binding energy (differences $\lesssim 0.1\%$). We outlined how the obtained fitting parameters, which effectively describe higher order PN orders, can be used for further waveform development.

For spinning, equal-mass systems, we extracted for the first time the individual spin contributions to the binding energy for black hole binaries. In particular we studied the spin-orbit, spin-spin, and cubic-in-spin terms. We find that while the spin-orbit interaction is accurately modeled with the EOB approximant, the spin-spin interaction of the SEOBNR model [34] as extracted by our method does not agree well with the NR results. in contrast to the uncalibrated EOB model. This is likely due to the structure of the spin-spin calibration parameters in the SEOBNR model that incorporate contributions from higher-order terms. For further development, a calibration with respect to the binding energy may improve the agreement further and allow an efficient way of decoupling conservative from dissipative dynamics.

Finally, considering a large set of unequal mass systems with aligned spin we again verified the good agreement of the full NR simulations and the EOB model. Extraction spin-orbit and spin-spin contributions permit analysis of the effect of the particular choice of the binaries effective spin parameter. We found best performance for the phase effective spin, χ_ϕ compared to the purely mass-weighted effective spin or the effective spin as it appears at leading order in the Hamiltonian. Additionally, we also presented a phenomenological representation of the spin-orbit contribution to the binding energy. For the considered cases, the error of the phenomenological fit is on the order of 1% during the inspiral and below 6% at merger.

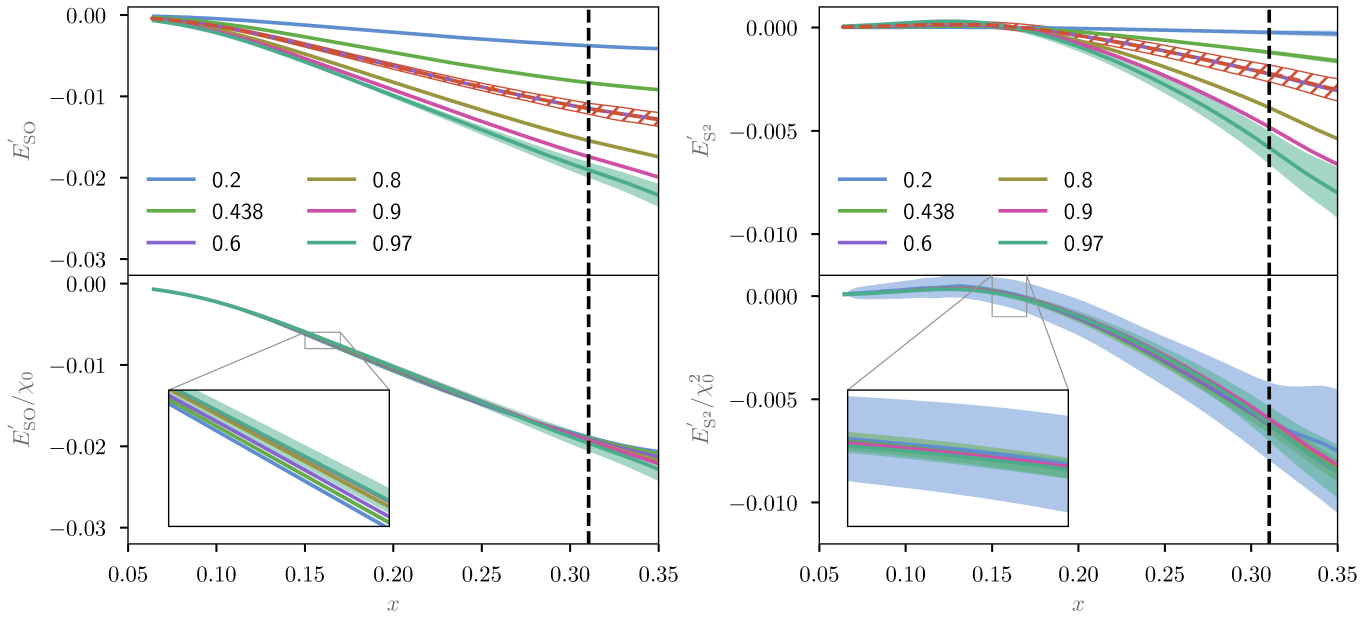

FIG. 18. Left: the approximate SO contribution to the binding energy, E'_{SO}, for all equal-spin cases described in Table III. The top panel shows the raw curves, and the bottom panel shows the results rescaled by χ. Right: the combination of spin-squared contributions, E'_{S^2}. The panels are the same as in the left plot, but rescaling is done by χ^2. Note that in both panels the rescaling causes the curves to lie very close to each other, indicating that the procedure is successful in isolating the corresponding contributions to the binding energy. The hatched area shows the error in the corresponding combinations as shown in Fig. 7, demonstrating that the simpler combinations yield smaller errors.

Appendix A: Extracting spin contributions from a small number of simulations

Extracting the contributions to binding energy as described in Sec. IV A requires a set of five configurations to determine the value for one spin magnitude. This amount of simulations is not available for all spin magnitudes, and performing these simulations is computationally expensive. Therefore, we show that for a wide range of spins, alternative expressions can be used to derive the SO and SS contributions using only two simulations per spin magnitude. In particular, consider

$$E'_{SO} = \frac{1}{4}\left(E(\nu,\chi_1,\chi_2) - E(\nu,-\chi_1,-\chi_2)\right), \quad \text{(A1)}$$

$$E'_{S^2} = \frac{1}{4}\left(E(\nu,\chi_1,\chi_2) + E(\nu,-\chi_1,-\chi_2)\right) - \frac{1}{2}E(\nu,0,0). \quad \text{(A2)}$$

Since only two (three) simulations are necessary to extract the linear (quadratic) in spin contributions, in contrast to Eqs. (18), results are less noisy.

To test Eq. (A1) and Eq. (A2) we show in Figure 18 the SO and SS contributions for a variety of equal mass cases. If the spin-orbit (spin-squared) contributions were extracted correctly, then they should scale linearly (quadratically) with the spin magnitude. This is indeed the case, as the rescaled curves lie virtually on top of each other, as shown in the bottom panels of Figure 18. The hatched red area shows the NR error from Figure 7 which is larger than the estimate of the NR error as computed from Eqs. (A1),(A2). Thus we see that this method performs as expected across a wider variety of spin-magnitudes and allows the approximate extraction of linear and quadratic in spin terms.

Appendix B: Configurations

SXS ID	q	SXS ID	q
0180	1.0	0007	1.5
0169	2.0	0259	2.5
0168	3.0	0167	4.0
0295	4.5	0056	5.0
0296	5.5	0297	6.5
0298	7.0	0299	7.5
0063	8.0	0300	8.5
0301	9.0	0302	9.5
0303	10.0	-	-
0201	2.32	0166	6.0
0199	8.73	0189	9.17

TABLE II. All non-spinning configurations used in this work. The top half of the table was used to construct the fit, while the bottom provided validation cases for the phenomenological fit.

SXS ID	q	χ_1	χ_2	SXS ID	q	χ_1	χ_2
1137	1.0	-0.970	-0.970	0159	1.0	-0.900	-0.900
0212	1.0	-0.800	-0.800	0215	1.0	-0.600	-0.600
0148	1.0	-0.438	-0.438	0149	1.0	-0.200	-0.200
0180	1.0	0.000	0.000	0150	1.0	0.200	0.200
1122	1.0	0.438	0.438	0228	1.0	0.600	0.600
0230	1.0	0.800	0.800	0160	1.0	0.900	0.900
0158	1.0	0.970	0.970	-	-	-	-
0214	1.0	-0.625	-0.25	0219	1.0	-0.500	0.90
0221	1.0	-0.400	0.80	0226	1.0	0.500	-0.90
0229	1.0	0.650	0.25	0232	1.0	0.900	0.50

TABLE III. Equal mass spinning cases used in this work. Configurations in the bottom half of the table are only used for validation.

ACKNOWLEDGMENTS

It is a pleasure to thank Sebastiano Bernuzzi, Alessandra Buonanno, Roberto Cotesta, Ian Hinder, Sylvain Marsat, Maarten van de Meent, Alessandro Nagar, Noah Sennett, Jan Steinhoff and Justin Vines for helpful discussions. We thank Alessandro Nagar for providing the E-j curves based on the EOB code presented in [30]. We acknowledge the support of the SXS collaboration and emphasize the importance of the public catalog [40]. Our work at Cal State Fullerton was supported in part by grants NSF PHY-1307489, PHY-1606522, and PHY-1654359. The computations were done on ORCA, which is supported in part by Cal State Fullerton, the Research Corporation for Science Advancement, and NSF PHY-1429873.

SXS ID	q	χ_1	χ_2	SXS ID	q	χ_1	χ_2
0233	2.00	-0.871	0.850	0234	2.00	-0.850	-0.850
0236	2.00	-0.600	0.000	0237	2.00	-0.600	0.600
0235	2.00	-0.600	-0.600	0238	2.00	-0.500	-0.500
0239	2.00	-0.371	0.850	0240	2.00	-0.300	-0.300
0241	2.00	-0.300	0.000	0242	2.00	-0.300	0.300
0243	2.00	-0.129	-0.850	0247	2.00	0.000	0.600
0246	2.00	0.000	0.300	0245	2.00	0.000	-0.300
0244	2.00	0.000	-0.600	0248	2.00	0.129	0.850
0251	2.00	0.300	0.300	0250	2.00	0.300	0.000
0249	2.00	0.300	-0.300	0252	2.00	0.371	-0.850
0253	2.00	0.500	0.500	0256	2.00	0.600	0.600
0255	2.00	0.600	0.000	0254	2.00	0.600	-0.600
0257	2.00	0.850	0.850	0258	2.00	0.871	-0.850
0260	3.00	-0.850	-0.850	0261	3.00	-0.731	0.850
0264	3.00	-0.600	-0.600	0265	3.00	-0.600	-0.400
0262	3.00	-0.600	0.000	0266	3.00	-0.600	0.400
0263	3.00	-0.600	0.600	0267	3.00	-0.500	-0.500
0105	3.00	-0.500	0.000	0268	3.00	-0.400	-0.600
0269	3.00	-0.400	0.600	0270	3.00	-0.300	-0.300
0271	3.00	-0.300	0.000	0272	3.00	-0.300	0.300
0273	3.00	-0.269	-0.850	0274	3.00	-0.231	0.850
0278	3.00	0.000	0.600	0275	3.00	0.000	-0.600
0277	3.00	0.000	0.300	0276	3.00	0.000	-0.300
0279	3.00	0.231	-0.850	0280	3.00	0.269	0.850
0281	3.00	0.300	-0.300	0282	3.00	0.300	0.000
0283	3.00	0.300	0.300	0284	3.00	0.400	-0.600
0285	3.00	0.400	0.600	0174	3.00	0.500	0.000
0286	3.00	0.500	0.500	0291	3.00	0.600	0.600
0288	3.00	0.600	-0.400	0287	3.00	0.600	-0.600
0289	3.00	0.600	0.000	0290	3.00	0.600	0.400
0292	3.00	0.731	-0.850	0293	3.00	0.850	0.850
0109	5.00	-0.500	0.000	0110	5.00	0.500	0.000
0207	7.00	-0.600	0.000	0206	7.00	-0.400	0.000
0204	7.00	0.400	0.000	0202	7.00	0.600	0.000
0064	8.00	-0.500	0.000	0065	8.00	0.500	0.000

TABLE IV. All unequal mass, spinning binaries used in this work. Cases with an asterisc were only used for validation.

[1] B. P. Abbott *et al.* (Virgo, LIGO Scientific), Phys. Rev. Lett. **116**, 061102 (2016), arXiv:1602.03837 [gr-qc].

[2] B. P. Abbott *et al.* (Virgo, LIGO Scientific), Phys. Rev. Lett. **116**, 241103 (2016), arXiv:1606.04855 [gr-qc].

[3] B. P. Abbott *et al.* (VIRGO, LIGO Scientific), Phys. Rev. Lett. **118**, 221101 (2017), arXiv:1706.01812 [gr-qc].

[4] B. P. Abbott *et al.* (Virgo, LIGO Scientific), Phys. Rev. Lett. **119**, 141101 (2017), arXiv:1709.09660 [gr-qc].

[5] B. P. Abbott *et al.* (Virgo, LIGO Scientific), (2017), arXiv:1711.05578 [astro-ph.HE].

[6] B. P. Abbott *et al.* (Virgo, LIGO Scientific), Phys. Rev. Lett. **119**, 161101 (2017), arXiv:1710.05832 [gr-qc].

[7] B. P. Abbott *et al.* (Virgo, LIGO Scientific), Phys. Rev. **X6**, 041015 (2016), arXiv:1606.04856 [gr-qc].

[8] J. Blackman, S. E. Field, C. R. Galley, B. Szilágyi, M. A. Scheel, M. Tiglio, and D. A. Hemberger, Phys. Rev. Lett. **115**, 121102 (2015), arXiv:1502.07758 [gr-qc].

[9] J. Blackman, S. E. Field, M. A. Scheel, C. R. Galley, C. D. Ott, M. Boyle, L. E. Kidder, H. P. Pfeiffer, and B. Szilágyi, (2017), arXiv:1705.07089 [gr-qc].

[10] P. Ajith *et al.*, *Gravitational wave data analysis. Proceedings: 11th Workshop, GWDAW-11, Potsdam, Germany, Dec 18-21, 2006*, Class. Quant. Grav. **24**, S689 (2007), arXiv:0704.3764 [gr-qc].

[11] P. Ajith *et al.*, Phys. Rev. Lett. **106**, 241101 (2011), arXiv:0909.2867 [gr-qc].
[12] M. Hannam, P. Schmidt, A. Bohé, L. Haegel, S. Husa, F. Ohme, G. Pratten, and M. Pürrer, Phys. Rev. Lett. **113**, 151101 (2014), arXiv:1308.3271 [gr-qc].
[13] L. Blanchet, Living Rev. Rel. **17**, 2 (2014), arXiv:1310.1528 [gr-qc].
[14] A. Buonanno and T. Damour, Phys. Rev. **D59**, 084006 (1999), arXiv:gr-qc/9811091 [gr-qc].
[15] T. Damour, P. Jaranowski, and G. Schaefer, Phys. Rev. **D62**, 084011 (2000), arXiv:gr-qc/0005034 [gr-qc].
[16] T. Damour, Phys. Rev. **D64**, 124013 (2001), arXiv:gr-qc/0103018 [gr-qc].
[17] A. Buonanno, Y. Chen, and T. Damour, Phys. Rev. **D74**, 104005 (2006), arXiv:gr-qc/0508067 [gr-qc].
[18] T. Damour, P. Jaranowski, and G. Schaefer, Phys. Rev. **D78**, 024009 (2008), arXiv:0803.0915 [gr-qc].
[19] T. Damour, B. R. Iyer, and A. Nagar, Phys. Rev. **D79**, 064004 (2009), arXiv:0811.2069 [gr-qc].
[20] T. Damour and A. Nagar, Phys. Rev. **D79**, 081503 (2009), arXiv:0902.0136 [gr-qc].
[21] E. Barausse, E. Racine, and A. Buonanno, Phys. Rev. **D80**, 104025 (2009), [Erratum: Phys. Rev.D85,069904(2012)], arXiv:0907.4745 [gr-qc].
[22] E. Barausse and A. Buonanno, Phys. Rev. **D81**, 084024 (2010), arXiv:0912.3517 [gr-qc].
[23] Y. Pan, A. Buonanno, R. Fujita, E. Racine, and H. Tagoshi, Phys. Rev. **D83**, 064003 (2011), [Erratum: Phys. Rev.D87,no.10,109901(2013)], arXiv:1006.0431 [gr-qc].
[24] E. Barausse, A. Buonanno, and A. Le Tiec, Phys. Rev. **D85**, 064010 (2012), arXiv:1111.5610 [gr-qc].
[25] T. Damour, A. Nagar, and S. Bernuzzi, Phys. Rev. **D87**, 084035 (2013), arXiv:1212.4357 [gr-qc].
[26] Y. Pan, A. Buonanno, M. Boyle, L. T. Buchman, L. E. Kidder, H. P. Pfeiffer, and M. A. Scheel, Phys. Rev. **D84**, 124052 (2011), arXiv:1106.1021 [gr-qc].
[27] Y. Pan, A. Buonanno, A. Taracchini, L. E. Kidder, A. H. Mroué, H. P. Pfeiffer, M. A. Scheel, and B. Szilágyi, Phys. Rev. **D89**, 084006 (2014), arXiv:1307.6232 [gr-qc].
[28] A. Taracchini *et al.*, Phys. Rev. **D89**, 061502 (2014), arXiv:1311.2544 [gr-qc].
[29] T. Damour and A. Nagar, Phys. Rev. **D90**, 044018 (2014), arXiv:1406.6913 [gr-qc].
[30] A. Nagar, T. Damour, C. Reisswig, and D. Pollney, Phys. Rev. **D93**, 044046 (2016), arXiv:1506.08457 [gr-qc].
[31] A. Nagar and A. Shah, Phys. Rev. **D94**, 104017 (2016), arXiv:1606.00207 [gr-qc].
[32] D. Bini and T. Damour, Phys. Rev. **D93**, 104040 (2016), arXiv:1603.09175 [gr-qc].
[33] S. Babak, A. Taracchini, and A. Buonanno, Phys. Rev. **D95**, 024010 (2017), arXiv:1607.05661 [gr-qc].
[34] A. Bohé *et al.*, Phys. Rev. **D95**, 044028 (2017), arXiv:1611.03703 [gr-qc].
[35] T. Damour, A. Nagar, D. Pollney, and C. Reisswig, Phys. Rev. Lett. **108**, 131101 (2012), arXiv:1110.2938 [gr-qc].
[36] `http://www.black-holes.org/SpEC.html`.
[37] M. A. Scheel, H. P. Pfeiffer, L. Lindblom, L. E. Kidder, O. Rinne, and S. A. Teukolsky, Phys. Rev. **D74**, 104006 (2006), arXiv:gr-qc/0607056 [gr-qc].
[38] B. Szilagyi, L. Lindblom, and M. A. Scheel, Phys. Rev. **D80**, 124010 (2009), arXiv:0909.3557 [gr-qc].
[39] L. T. Buchman, H. P. Pfeiffer, M. A. Scheel, and B. Szilagyi, Phys. Rev. **D86**, 084033 (2012), arXiv:1206.3015 [gr-qc].
[40] `http://www.black-holes.org/waveforms`.
[41] A. H. Mroue *et al.*, Phys. Rev. Lett. **111**, 241104 (2013), arXiv:1304.6077 [gr-qc].
[42] G. Lovelace, R. Owen, H. P. Pfeiffer, and T. Chu, Phys. Rev. **D78**, 084017 (2008), arXiv:0805.4192 [gr-qc].
[43] H. P. Pfeiffer and J. W. York, Jr., Phys. Rev. **D67**, 044022 (2003), arXiv:gr-qc/0207095 [gr-qc].
[44] H. P. Pfeiffer, L. E. Kidder, M. A. Scheel, and S. A. Teukolsky, Comput. Phys. Commun. **152**, 253 (2003), arXiv:gr-qc/0202096 [gr-qc].
[45] L. Lindblom, M. A. Scheel, L. E. Kidder, R. Owen, and O. Rinne, Class. Quant. Grav. **23**, S447 (2006), arXiv:gr-qc/0512093 [gr-qc].
[46] F. Pretorius, Phys. Rev. Lett. **95**, 121101 (2005), arXiv:gr-qc/0507014 [gr-qc].
[47] H. Friedrich, Comm. Math. Phys. **100**, 525 (1985).
[48] L. Lindblom and B. Szilagyi, Phys. Rev. **D80**, 084019 (2009), arXiv:0904.4873 [gr-qc].
[49] D. A. Hemberger, M. A. Scheel, L. E. Kidder, B. Szilágyi, G. Lovelace, N. W. Taylor, and S. A. Teukolsky, Class. Quant. Grav. **30**, 115001 (2013), arXiv:1211.6079 [gr-qc].
[50] M. A. Scheel, M. Giesler, D. A. Hemberger, G. Lovelace, K. Kuper, M. Boyle, B. Szilágyi, and L. E. Kidder, Class. Quant. Grav. **32**, 105009 (2015), arXiv:1412.1803 [gr-qc].
[51] B. Szilágyi, Int. J. Mod. Phys. **D23**, 1430014 (2014), arXiv:1405.3693 [gr-qc].
[52] B. Szilágyi, J. Blackman, A. Buonanno, A. Taracchini, H. P. Pfeiffer, M. A. Scheel, T. Chu, L. E. Kidder, and Y. Pan, Phys. Rev. Lett. **115**, 031102 (2015), arXiv:1502.04953 [gr-qc].
[53] K. Barkett *et al.*, Phys. Rev. **D93**, 044064 (2016), arXiv:1509.05782 [gr-qc].
[54] G. Lovelace *et al.*, Class. Quant. Grav. **32**, 065007 (2015), arXiv:1411.7297 [gr-qc].
[55] M. Ruiz, R. Takahashi, M. Alcubierre, and D. Nunez, Gen. Rel. Grav. **40**, 2467 (2008), arXiv:0707.4654 [gr-qc].
[56] S. Bernuzzi, T. Dietrich, W. Tichy, and B. Brügmann, Phys. Rev. **D89**, 104021 (2014), arXiv:1311.4443 [gr-qc].
[57] T. Dietrich, S. Bernuzzi, M. Ujevic, and W. Tichy, Phys. Rev. **D95**, 044045 (2017), arXiv:1611.07367 [gr-qc].
[58] T. Dietrich, S. Bernuzzi, B. Bruegmann, M. Ujevic, and W. Tichy, (2017), arXiv:1712.02992 [gr-qc].
[59] M. Levi and J. Steinhoff, (2016), arXiv:1607.04252 [gr-qc].
[60] G. Lovelace *et al.*, Class. Quant. Grav. **33**, 244002 (2016), arXiv:1607.05377 [gr-qc].
[61] P. Kumar, K. Barkett, S. Bhagwat, N. Afshari, D. A. Brown, G. Lovelace, M. A. Scheel, and B. Szilágyi, Phys. Rev. **D92**, 102001 (2015), arXiv:1507.00103 [gr-qc].
[62] M. Boyle, Phys. Rev. **D87**, 104006 (2013), arXiv:1302.2919 [gr-qc].
[63] M. Boyle and A. H. Mroue, Phys. Rev. **D80**, 124045 (2009), arXiv:0905.3177 [gr-qc].
[64] T. Chu, H. Fong, P. Kumar, H. P. Pfeiffer, M. Boyle, D. A. Hemberger, L. E. Kidder, M. A. Scheel, and B. Szilagyi, Class. Quant. Grav. **33**, 165001 (2016), arXiv:1512.06800 [gr-qc].
[65] N. W. Taylor, M. Boyle, C. Reisswig, M. A. Scheel, T. Chu, L. E. Kidder, and B. Szilágyi, Phys. Rev. **D88**, 124010 (2013), arXiv:1309.3605 [gr-qc].
[66] A. Le Tiec, E. Barausse, and A. Buonanno, Phys. Rev. Lett. **108**, 131103 (2012), arXiv:1111.5609 [gr-qc].
[67] T. Damour, P. Jaranowski, and G. Schäfer, Phys. Rev.

D89, 064058 (2014), arXiv:1401.4548 [gr-qc].
[68] S. J. Kapadia, N. K. Johnson-McDaniel, and P. Ajith, Phys. Rev. **D93**, 024006 (2016), arXiv:1509.06366 [gr-qc].
[69] M. Campanelli, C. O. Lousto, and Y. Zlochower, Phys. Rev. **D74**, 041501 (2006), arXiv:gr-qc/0604012 [gr-qc].